Nano-engineering the evolution of skyrmion crystal in synthetic antiferromagnets

Cite as: Appl. Phys. Rev. **9**, 021404 (2022); https://doi.org/10.1063/5.0081455
Submitted: 09 December 2021 • Accepted: 29 March 2022 • Published Online: 12 April 2022

Mangyuan Ma, Ke Huang, Yong Li, et al.

COLLECTIONS

EP This paper was selected as an Editor's Pick

Applied Physics Reviews ARTICLE scitation.org/journal/are

Nano-engineering the evolution of skyrmion crystal in synthetic antiferromagnets

Cite as: Appl. Phys. Rev. **9**, 021404 (2022); doi: 10.1063/5.0081455
Submitted: 9 December 2021 · Accepted: 29 March 2022 ·
Published Online: 12 April 2022

View Online Export Citation CrossMark

Mangyuan Ma,[1] Ke Huang,[2] Yong Li,[1] Sihua Li,[2] Qiyuan Feng,[3] Calvin Ching Ian Ang,[2] Tianli Jin,[2] Yalin Lu,[3] Qingyou Lu,[3] Wen Siang Lew,[2,a)] Fusheng Ma,[1,a)] and X. Renshaw Wang[2,4,a)]

AFFILIATIONS

[1]Jiangsu Key Laboratory of Opto-Electronic Technology, Center for Quantum Transport and Thermal Energy Science, School of Physics and Technology, Nanjing Normal University, Nanjing 210046, China

[2]Division of Physics and Applied Physics, School of Physical and Mathematical Sciences, Nanyang Technological University, 21 Nanyang Link, Singapore 637371, Singapore

[3]Anhui Province Key Laboratory of Condensed Matter Physics at Extreme Conditions, High Magnetic Field Laboratory, Chinese Academy of Sciences, Hefei 230031, China

[4]School of Electrical and Electronic Engineering, Nanyang Technological University, 50 Nanyang Ave, Singapore 639798, Singapore

[a)]**Authors to whom correspondence should be addressed:** phymafs@njnu.edu.cn; wensiang@ntu.edu.sg; and renshaw@ntu.edu.sg

ABSTRACT

The evolution of skyrmion crystals encapsulates skyrmion's critical behaviors, such as nucleation, deformation, and annihilation. Here, we achieve a tunable evolution of artificial skyrmion crystals in nanostructured synthetic antiferromagnet multilayers, which are composed of perpendicular magnetic multilayers and nanopatterned arrays of magnetic nanodots. The out-of-plane magnetization hysteresis loops and first-order reversal curves show that the nucleation and annihilation of the artificial skyrmion can be controlled by tuning the diameter of and spacing between the nanodots. Moreover, when the bottom layer thickness increases, the annihilation of skyrmion shifts from evolving into a ferromagnetic spin texture to evolving into an antiferromagnetic spin texture. Most significantly, nonvolatile multiple states are realized at zero magnetic field via controlling the proportion of the annihilated skyrmions in the skyrmion crystal. Our results demonstrate the tunability and flexibility of the artificial skyrmion platform, providing a promising route to achieve skyrmion-based multistate devices, such as neuromorphic spintronic devices.

I. INTRODUCTION

A magnetic skyrmion is a topologically protected spin texture with nontrivial spin configurations.[1–4] It was first observed in non-centrosymmetric B20 compound MnSi at a low temperature, about 29 K,[5] and was stabilized by an external magnetic field and bulk Dzyaloshinskii–Moriya interaction (DMI).[6–8] It was found that other bulk magnets with non-centrosymmetry and DMI can also host skyrmion configurations.[9–14] Alternatively, the existence of skyrmions in nanometer-thick multilayers with interfacial DMI was also theoretically predicted[15,16] and experimentally observed in the Ta/CoFeB/TaO_x multilayer.[17] Since then, magnetic multilayers consisting of ferromagnets and heavy metals become promising and attractive skyrmion platforms.[17–22] In particular, the room-temperature yet zero-field skyrmion can nucleate and exist stably in this platform of multilayers, facilitating the development of practical skyrmion-based spintronic devices.[23–26] Because of their topological stability, nanoscale size, and low driven current, magnetic skyrmions are highly promising for both fundamental studies and spintronic applications,[27–32] such as racetrack memory,[33,34] logic devices,[35,36] and skyrmion magnonic crystals.[37–40]

Incorporating skyrmions into advanced artificial structures, such as nanoribbons,[41–43] nanowires,[44,45] nanodots,[46,47] and hybrid nanodot-film structures,[48–53] is an emerging trend in the investigation of the skyrmionic field. Although the nano-patterns inevitably limit their motion along racetracks resulting from the pinning effect, skyrmions can in turn locally oscillate in nanodots.[47,54,55] Most importantly, in contrast to the spontaneous nucleation in bulk materials and continuous magnetic multilayers, skyrmions in nano-patterned multilayers exhibit higher existence stability, position controllability, and even a crystal order. The crystal-like group formed by these periodic skyrmions is referred to as the skyrmion lattice[50,56] or skyrmion crystal.[48,56,57] Recently, the idea of endowing the skyrmion array with an artificial crystal order attracts much research attention and expands the spintronic research frontier.[37,38] However, to enhance and exploit the functionalities of the skyrmion crystals, introducing engineered spin textures into the skyrmion crystals is desirable yet elusive.

To construct a skyrmion crystal, there are typically two types of skyrmions, namely, conventional skyrmion induced by DMI and artificial skyrmion induced by interlayer interaction.[48–50,56] In particular, the artificial skyrmion crystal gains more functionalities due to the extra tunability from the interface.[58–64] Previous works have demonstrated that artificial skyrmion crystals can be formed via the interfacial ferromagnetic coupling between the top magnetic nanodots and the bottom multilayer with perpendicular magnetic anisotropy,[58–61] or via the exchange bias in the ferromagnet/antiferromagnet multilayers.[62–64] Recently, antiferromagnetic interlayer exchange coupling (AFM-IEC) in a synthetic antiferromagnet (SAF) has drawn much attention due to its capabilities in stabilizing skyrmions or generating functional spin textures.[65–70] Therefore, engineering the artificial skyrmion crystal in SAF nanostructures might introduce controlled spin textures, permit unseen functionalities, and boost the control of skyrmions.

In this work, we engineer the SAF into nanostructures, which contain the top nanodots and the continuous bottom layer with varied geometries. A periodically ordered skyrmion crystal is generated in these nanostructures. The out-of-plane magnetization hysteresis (m_z–H) loops and first-order reversal curves (FORCs) reveal that the evolutions of the skyrmion crystal, which are nucleation and annihilation, strongly depend on the thicknesses of the bottom magnetic layer and the diameters of the top nanodots. Especially, by increasing the thickness of the bottom layer, skyrmions can be switched from evolving into a ferromagnetic to an antiferromagnetic spin texture. We also find that even with part of the skyrmion crystal evolving into other spin textures, the rest is still stable. Based on this feature, we achieve nonvolatile multiple states, characterized by multiple levels of Hall resistance.

II. RESULTS AND DISCUSSION

Figure 1(a) shows the schematic structure of the nanostructured SAF multilayers Ta(4)/Pt(4)/[Pt(0.6)/Co(0.6)]$_N$/Ru(0.9)/[Co(0.6)/Pt(0.6)]$_4$/Ta(4), where the numbers in parentheses are the nominal layer thickness in nanometer. Detailed information of sample preparation can be found in Sec. IV. The spacing layer Ru provides an AFM-IEC between the bottom [Pt/Co]$_N$ and top [Co/Pt]$_4$ layers. The top Ta layer is used to prevent oxidation, and the bottom Ta and Pt layers work as seeding layers. The bottom [Pt/Co]$_N$ layer has a repeating number N ($N = 2$ or 4). Note that the repeating number $N = 2$ or 4 ensures a single-magnetic-domain state in the bottom [Pt/Co]$_N$ layer. When N takes a larger value, the domain in the magnetic layer may exhibit a multi-domain state,[71–74] which is unfavorable in this work. The top [Co/Pt]$_4$ layer was etched into circular nanodots with

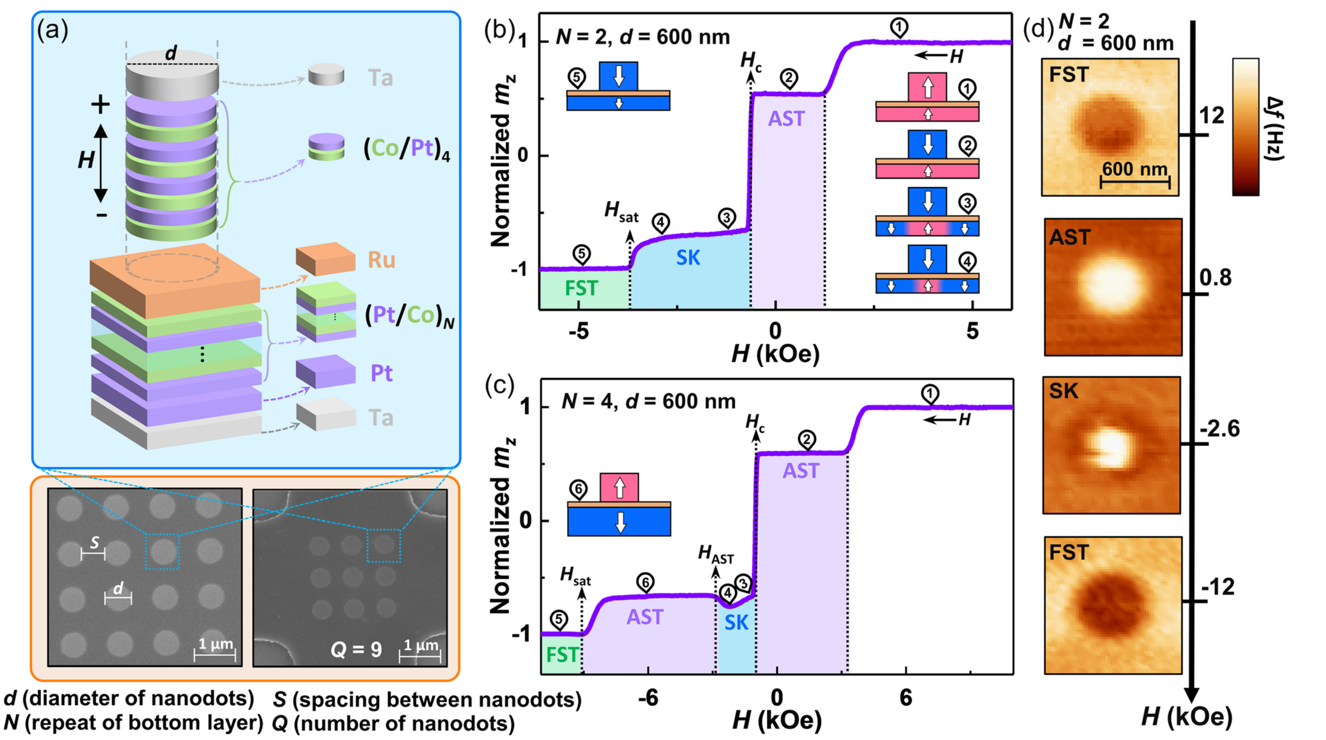

FIG. 1. Magnetization switching processes of nanostructured SAF multilayers. (a) Schematic illustration of nanostructured SAF multilayers. Bottom left and bottom right images are the SEM images of a 2D arrangement of the top nanodots with diameter $d = 600$ nm and a Hall bar with nine top nanodots with diameter $d = 400$ nm, respectively. (b) and (c) MOKE-measured descending branches of m_z–H loops of nanostructured SAF multilayers with $d = 600$ nm for $N = 2$ (b) and 4 (c). Insets are cross-section views of magnetization distributions at selected fields. (d) MFM images of nanostructured SAF multilayers with $N = 2$ and $d = 600$ nm at typical fields. The fields are selected at positive FST, AST, SK, and negative FST states. The MFM contrast, which is caused by the resonant frequency shift (Δf) of the MFM cantilever, shows a dark/bright contrast when the interaction between the MFM tip and the local magnetization of the sample is attractive/repulsive.

diameters (d) varying from 100 to 600 nm. In all samples, the spacing between the nanodots (S) is equal to d. We prepared the nanostructured SAF multilayers with two types of nanodot distributions, namely, (i) two-dimensional arrangement of nanodots for magneto-optical Kerr effect (MOKE) measurement [see the scanning electron microscopy (SEM) image of $d = 600$ nm at the bottom left of Fig. 1(a)] and (ii) a finite number of nanodots (Q) for Hall resistance measurement [see the SEM image of $d = 400$ nm at the bottom right of Fig. 1(a) for $Q = 9$]. Note that $Q = 0$ is the sample with continuous ferromagnetic multilayers $[Pt/Co]_N$, and it serves as a reference sample. The schematics of the samples for MOKE and Hall resistance measurements can be found in Sec. II of the supplementary material. We define the upward and downward directions as the positive and negative directions of the external magnetic field, respectively [Fig. 1(a)].

The m_z–H loops of nanostructured SAF multilayers were measured by MOKE. Technical details of the MOKE measurement are presented in Sec. IV. Figures 1(b) and 1(c) show the descending branches of the MOKE-measured m_z-H loops of the nanostructured SAF multilayers with $d = 600$ nm for $N = 2$ and $N = 4$, respectively. Both of the m_z–H loops exhibit multi-step switching, which corresponds to different magnetization distributions.[53] We define the coercive field (H_c) as the magnetic field value at which the m_z crosses zero (see Sec. III of the supplementary material). Additionally, to identify all the magnetization states, we performed magnetic force microscopy (MFM) measurements on the nanostructured SAF multilayers with $N = 2$, $d = 600$ nm at various fields. Figure 1(d) shows the measured typical MFM images at selected fields ($H = 12$, 0.8, -2.6, and -12 kOe) for different magnetization states. Technical details of the MFM measurement are presented in Sec. IV. We found that, along the descending branch of the m_z–H loop, the nanostructure with $N = 2/4$ and $d = 600$ nm sequentially experiences four/five distinct magnetization states. In order to elaborate the different magnetic transitions clearly for $N = 2/4$, we presented six examples of cross section views of magnetization distribution at different magnetization states, which are labeled by numbers from 1 to 6 on the m_z–H loops [insets of Figs. 1(b) and 1(c)].

We now first focus on the process of magnetization switching of the $N = 2$, $d = 600$ nm samples [Fig. 1(b)]. When the external field is larger than the saturation field (H_{sat}), the magnetization of the top and bottom layers is aligned along the direction of the external field [inset 1 of Fig. 1(b)]. As the external field decreases toward 0 kOe, the magnetization of the top nanodots is reversed by the AFM-IEC [inset 2 of Fig. 1(b)]. Because the magnetizations of the top nanodots and the bottom continuous layer are antiparallel, we denote this magnetization configuration as an antiferromagnetic spin texture (AST) state. When the negative external field is greater than the coercive field (H_c), the magnetization of the dot-uncovered region of the bottom layer is reversed downward. The magnetization of the dot-covered region remains antiparallel to that of the top nanodots because of the AFM-IEC. Considering solely the bottom continuous layer, a skyrmion-like magnetization configuration nucleates [inset 3 of Fig. 1(b)], which is referred to as a skyrmion (SK) state. Further increasing the external field negatively will gradually offset the AFM-IEC protection, resulting in a shrinking annihilation of the skyrmion [inset 4 of Fig. 1(b)]. Because the negative external field is larger than H_{sat}, the magnetization of the bottom layer is fully reversed downward, and this state is referred to as a ferromagnetic spin texture (FST) state [inset 5 of Fig. 1(b)]. The MFM images shown in Fig. 1(d) reflect the magnetization configurations corresponding to the four representative states of the m_z–H loop in Fig. 1(b): (i) positive FST state ($H = 12$ kOe); (ii) AST state ($H = 0.8$ kOe); (iii) SK state ($H = -2.6$ kOe); and (iv) negative FST state ($H = -12$ kOe).

Similarly, Fig. 1(c) shows the magnetization evolution of nanostructured SAF multilayers with $N = 4$, $d = 600$ nm. In particular, an additional AST state with a rise of m_z occurs after the annihilation of the artificial skyrmions [inset 6 of Fig. 1(c)]. In comparison to the $N = 2$ nanostructure, the additional AST state is induced by a larger AFM-IEC in the $N = 4$ nanostructure. The difference of AFM-IEC between the $N = 2$ and $N = 4$ nanostructures is confirmed by comparing the m_z–H loops of continuous SAF multilayers with different N (Sec. IV of the supplementary material).

In order to investigate the effect of d on the nucleation and shrinking annihilation of skyrmions in nanostructured SAF multilayers, d was varied from 100 to 600 nm. Figures 2(a) and 2(b) show the fractions of the MOKE-measured m_z-H loops with various N and d as well as of the reference samples with continuous ferromagnetic $[Pt/Co]_2$ and $[Pt/Co]_4$ multilayers. The full m_z–H loops are shown in Sec. V of the supplementary material. The critical external field of skyrmion nucleation (H_c) decreases and gradually approaches the H_c of the reference samples, when d increases from 100 to 600 nm for both $N = 2$ and 4 samples. On the contrary, the critical external fields of skyrmion shrinking annihilation, which are H_{sat} for $N = 2$ and H_{AST} for $N = 4$, increase as d increases. The different dependence of H_c, $H_{sat,}$ and H_{AST} against d can be understood from the different switching scenarios of the bottom continuous $[Pt/Co]_N$ layer. Taking $N = 2$ as an example, Fig. 2(c) schematically shows that the nanostructured SAF multilayers can be divided into three regions, namely, (a) the dot-covered region, (b) the dot-non-covered region, and (c) the top nanodots. When the external field negatively increases, the magnetization transitions of the AST-SK and the SK-FST manifest as the switching of regions B and A, respectively [Fig. 2(d)] The AST-SK magnetization transition is realized by the reversal of region B, which is collectively determined by three interactions: (i) the coercivity field ($H_{c\text{-}B}$) of the continuous bottom $[Pt/Co]_2$ layer, (ii) the ferromagnetic exchange interaction field ($H_{ex\text{-}AB}$) at the interface between regions A and B, and (iii) the external field (H). Figure 2(d) shows that, during the skyrmion nucleation, the magnetization of region B is reversed when H is larger than the AST-SK transition field (H_c). The value of H_c is decided by the summation of $H_{ex\text{-}AB}$ and $H_{c\text{-}B}$,

$$|H_c| = |H_{ex\text{-}AB}| + |H_{c\text{-}B}|, \qquad (1)$$

where both $H_{ex\text{-}AB}$ and $H_{c\text{-}B}$ protect the region B from being reversed by H. However, when $H = H_c$, the magnetization of region B reverse downward, the magnetization of region A is retained by the AFM-IEC between regions A and C. As a result, region A tends to protect the region B from being reversed by $H_{ex\text{-}AB}$. For a smaller d ($d = S$), the contribution of $H_{ex\text{-}AB}$ to H_c is relatively larger. While $H_{c\text{-}B}$ is dependent on the coercivity field of the continuous $[Pt/Co]_2$ layer but independent of d, the inverse dependence of H_c on d, therefore, can be understood according to Eq. (1).

On the other hand, the SK-FST magnetization transition is realized by the reversal of region A. This transition is collectively determined by four parameters: (i) the coercivity field ($H_{c\text{-}A}$) of the continuous bottom $[Pt/Co]_2$ layer, (ii) the ferromagnetic exchange interaction field ($H_{ex\text{-}BA}$) at the interface between regions A and B, (iii)

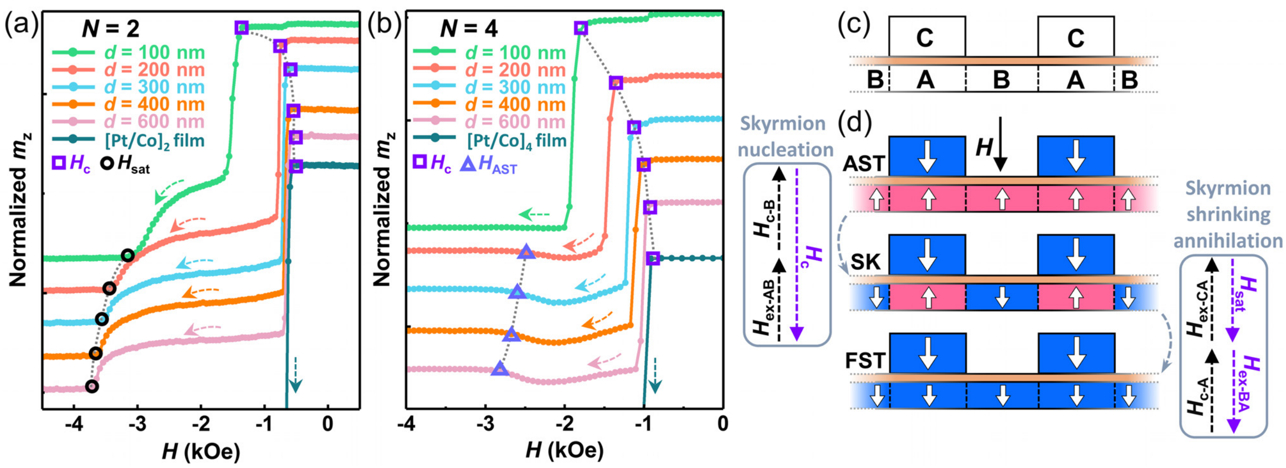

FIG. 2. Nucleation and shrinking annihilation of artificial skyrmions in nanostructured SAF multilayers. (a) and (b) Fractions of the descending branches of MOKE-measured m_z–H loops of nanostructured SAF multilayers with top nanodots of various diameters for $N = 2$ (a) and 4 (b). Open squares, circles, and triangles represent H_c, H_{sat}, and H_{AST}, respectively. (c) Cross section view of nanostructured SAF multilayers with $N = 2$. Regions A, B, and C are the dot-covered region, dot-non-covered region, and top nanodot region, respectively. (d) Magnetization switching of regions B and A during the AST-SK and the SK-FST transition processes.

the AFM-IEC field ($H_{ex\text{-}CA}$) between regions A and C, and (iv) H. Figure 2(d) shows that the skyrmion shrinks and annihilates where the magnetization of region A could be reversed and when H is larger than the SK-FST transition field H_{sat} of the SK-FST transition. The value of H_{sat} is determined by

$$|H_{sat}| = |H_{ex\text{-}CA}| + |H_{c\text{-}A}| - |H_{ex\text{-}BA}|, \tag{2}$$

where both $H_{ex\text{-}CA}$ and $H_{c\text{-}A}$ protect region A from being reversed by H. $H_{ex\text{-}CA}$ and $H_{c\text{-}A}$ are determined by the AFM-IEC strength and the coercivity field of the continuous [Pt/Co]$_2$ layer, respectively. However, both are independent of d. In contrast, region B tends to reverse region A via $H_{ex\text{-}BA}$. For a smaller d, the $H_{ex\text{-}BA}$ is relatively larger. Hence, the dependence of H_{sat} on d can be understood according to Eq. (2), and a smaller d results in a smaller H_{sat}. Similarly, the dependence of H_c and H_{AST} on d for $N = 4$ can also be understood by considering the field-dependent reversal of regions A, B, and C. Therefore, the field ranges of the SK state, which are $|H_{sat} - H_c|$ for $N = 2$ and $|H_{AST} - H_c|$ for $N = 4$, can be manipulated by tailoring d, and the tunability further enables the flexibility of the nanostructured SAF multilayers in skyrmionic and magnonic applications.

Furthermore, in contrast to the skyrmion's shrinking annihilation in the form of SK-FST and SK-AST transitions, skyrmions can also annihilate in a form of expansion. To investigate the skyrmion-expansion-induced magnetization transition, we measured minor m_z-H loops using MOKE, i.e., H_{sat}-H_R-H_{sat} loops, by choosing a reversal field $H_R < H_{sat}$. Figures 3(a) and 3(b) show minor loops of $d = 300$ nm samples with $N = 2$ and 4, respectively. Each figure contains two minor loops with H_R located in the SK state ($H_R = H_{R1}$) and FST/AST state ($H_R = H_{R2}$). We observed that the magnetization $m_z(H, H_R)$ is highly dependent on the selection of H_R, when the H increases from H_R toward H_{sat}. For instance, the corresponding cross sections of three loops with different H_R at $H = 2$ kOe are indicated by vertical dashed lines in Figs. 3(a) and 3(b). This difference in magnetization distribution originates from the H_R-dependent magnetization transition. When $H_R = H_{R1}$, the SK-AST transition occurs in both $N = 2$ and 4 samples together with a type of skyrmion annihilation in a form of expansion. When $H_R = H_{R2}$, the minor loops coincide with the ascending branches of major loops. Skyrmion nucleation occurs when the minor loops cross positive H_c.

Because the skyrmion-expansion-induced magnetization transition depends on the value of H_R, a systematic investigation of $m_z(H, H_R)$ is necessary. Here, we used the FORC technique for the detailed exploration. The FORC technique was used in the MOKE measurement by changing H_R with an interval of ΔH_R. The FORCs, which is composed of a large number of "H_{sat}-H_R-H_{sat}" minor loops,[75–77] have been widely used to study the distribution of switching fields, the interaction fields between neighboring domains, and the irreversibility of the magnetization switching mechanism.[78–80] Details of FORCs and calculation of the FORC diagram are described in Sec. VI of the supplementary material. Figures 3(c) and 3(d) show the fractions of MOKE-measured FORCs in the form of contour plots of $m_z(H, H_R)$ with d varying from 100 to 600 nm for $N = 2$ and 4 samples. The corresponding full FORCs and FORC diagrams can be found in Fig. S6 of the supplementary material. Depending on the values of H_R, there are two left-right boundaries in the contour plots of $m_z(H, H_R)$, and they are indicated as boundaries 1 and 2 in Figs. 3(c) and 3(d). Now, we use the minor loops and the contour plots of $m_z(H, H_R)$ for $N = 2$, $d = 300$ nm [Figs. 3(a) and 3(c)] to elaborate on the origins behind the presence of boundaries. When $H_R = H_{R1}$, boundary #1 corresponds to the SK-AST transition [insets of Fig. 3(c)]. As for $H_R = H_{R2}$, boundary #2 corresponds to the AST-SK transition [insets of Fig. 3(c)]. In addition, the position of boundary #1/#2 decreases/increases to low/high H when d decreases from 600 to 100 nm. This dependence of boundary position indicates that the skyrmions in larger d samples can expand continuously to the positive field region. On one hand, skyrmion can stabilize under zero field, when H_R locates at the SK state. On the other hand, the skyrmions can nucleate more easily when H_R locates at the FST state for the samples with larger d.

Figure 3(d) shows the contour plots of $m_z(H, H_R)$ for $N = 4$ sample with two left-right boundaries. Similar to the boundaries of $N = 2$

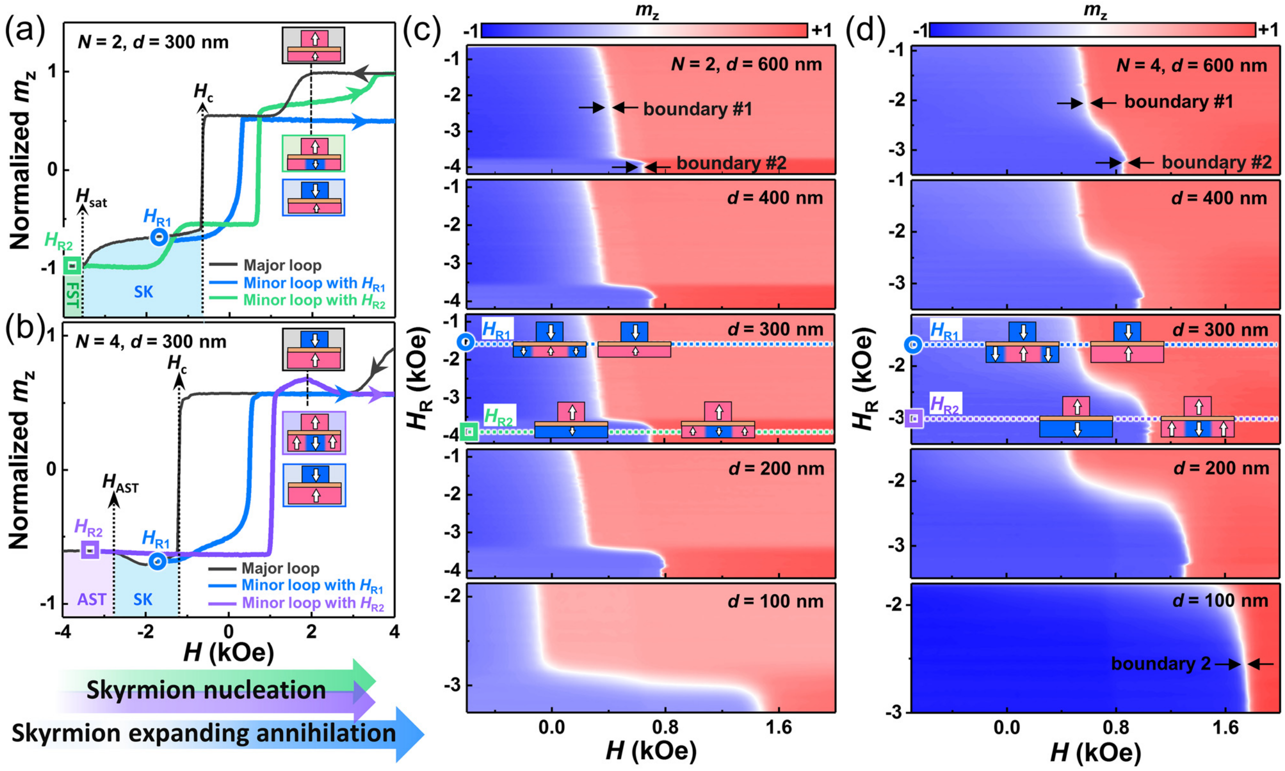

FIG. 3. MOKE-measured FORCs of the skyrmion nucleation and skyrmion expanding annihilation. (a) and (b) Fractions of major and minor m_z-H loops of nanostructured SAF multilayers with $d = 300$ nm for (a) $N = 2$ and (b) $N = 4$. Black, blue, and green (purple) solid lines represent the major loop, minor loop with H_{R1} selected at the SK state, and minor loop with H_{R2} selected at the FST (AST) state, respectively. Insets are the schematic cross sections of the three loops at $H = 2$ kOe. (c) and (d) Fractions of FORCs presented in the form of contour plots of $m_z(H, H_R)$ with various d in (c) $N = 2$ and (d) $N = 4$. Horizontal dash lines represent the evolutions of $m_z(H, H_R)$ along with the minor loops with H_{R1} (open circle) and H_{R2} (open square). Insets represent the SK-AST and the AST-SK transitions along with the minor loops with $H_R = H_{R1}$ and $H_R = H_{R2}$, respectively.

sample, the boundary #1/#2 corresponds to the SK-AST and the AST-SK transition for $N = 4$ sample by considering the minor loops in Fig. 3(b). The boundary #1/#2 of the $N = 4$ sample moves similarly to that of the $N = 2$ sample. Note that no boundary #1 occurs in $N = 4$ and $d = 100$ nm sample, indicating that an SK state hardly exists in this case. This is consistent with our experimental results of the m_z-H loop of $d = 100$ nm in Fig. 2(b).

So far, we have mainly focused on the intrinsic properties of skyrmions in the nanostructured SAF multilayers with various N and d. Now, we switch to Hall resistance measurements to investigate the potential applications based on the evolution of skyrmions. Figure 4(a) shows the evolution of the Hall resistance (R_{xy}) of the nanostructured SAF multilayers with fixed $N = 4$ and $d = 400$ nm, but varied $Q = 1$ and 9. In order to reveal the influence of Q on the behaviors of skyrmion, a zoomed-in view of the SK region is presented in Fig. 4(b). The SK region can be divided into stabilization and annihilation regions, which correspond to the shrinking of the skyrmion and the SK-AST transition, respectively. We found that the annihilation region of skyrmions in $Q = 9$ nanostructure is much larger than that in the $Q = 1$ nanostructure, which indicates that the nine skyrmions in the $Q = 9$ nanostructure annihilate asynchronously. Based on this phenomenon, we could purposely nucleate or annihilate different numbers of skyrmions to achieve multiple states at zero field. Note that the annihilation region manifests as a rise in the m_z–H loop [Fig. 1(c)] but a sharp drop in the Hall resistance hysteresis (R_{xy}-H) loop. This should be because Hall resistance measurement is more sensitive to the continuous bottom layer and less sensitive to the etched top layer.

To experimentally realize the multiple states based on the different numbers of skyrmions, we measured the reversal curves with the reversal fields H_R selected at different fields, where there are different numbers of skyrmions. Figure 4(c) shows a full major curve and three reversal curves with $H_R = -1.6$, -2.2, and -2.4 kOe. Figure 4(d) shows the zoomed-in view of the three reversal curves. Note that we only present the results of the descending branch. Similar states could also be achieved in the ascending branch of the positive field region. As shown in Fig. 4(d), we obtained four different states at zero field, namely, base state, state 1, state 2, and state 3. The base state was realized by sweeping the external field from $H_R = -H_{sat}$ to zero field, and there is no skyrmion at the H_R. State 1, 2, and 3 were achieved by sweeping the external field from different H_R to zero field, and there are different numbers of skyrmions at these selected H_R. Moreover, we conducted local hysteresis loops sweeping between H_R and zero field for the four states. The value of R_{xy} at zero field is always repeatable

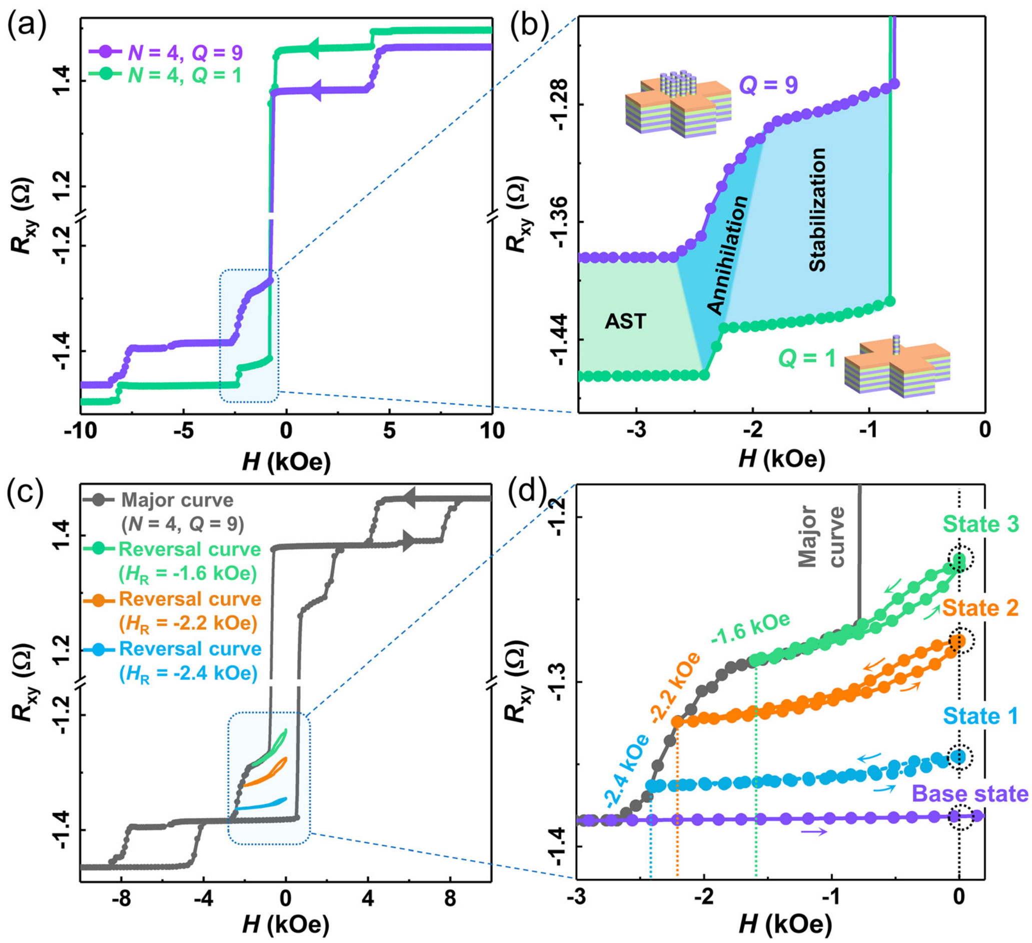

FIG. 4. Skyrmion-based nonvolatile multiple states. (a) Descending branches of R_{xy}-H loops of nanostructured SAF multilayers with $N = 4$, $Q = 1$ and 9. (b) Zoomed-in view of the region indicated by the blue frame in (a). Insets are the schematic illustration of nanostructured SAF multilayers with $Q = 1$ and 9. (c) Major and reversal curves of the nanostructured SAF multilayers with $N = 4$, $Q = 9$. (d) Zoomed-in view of the region indicated by the blue frame in (c). Dash line circles indicate the zero-field multiple states achieved by the reversal curves with different reversal fields: $H_R = -1.6$, -2.2, and -2.4 kOe.

[Fig. 4(d)], which indicates that the multiple states based on the different numbers of skyrmions are nonvolatile and robust.

We attribute these multiple states to an asynchronous evolution of the skyrmions with the external field. For the nanostructured SAF multilayers with the periodically arranged nanodots, the skyrmions forms in the bottom layer are also arranged periodically and behave the same as their neighbors. However, the nine skyrmions in the nanostructured SAF multilayers with $Q = 9$ can be divided into three types according to the difference in their positions: (i) four skyrmions at the corner, (ii) four skyrmions at the edge center, and (iii) one skyrmion at the center. The evolutions of the three types of skyrmions with the external field are different, which is confirmed by the micromagnetic simulation in Sec. VIII of the supplementary material (the relevant simulation parameters are given in Sec. I of the supplementary material). Our Hall resistance measurement and simulated results further demonstrate that, if we could introduce additional asymmetry of skyrmions through tailoring the shape, distribution, and size of the nanostructure, the nucleation and annihilation of skyrmion can be controlled more accurately.

III. CONCLUSION AND OUTLOOK

In summary, we experimentally investigated the behaviors of skyrmion crystals in the nanostructured SAF multilayers and validated a feasible scheme for the application of the multilayers. The existence of the skyrmion crystal in nanostructured SAF multilayers and its shrinking annihilation, i.e., the SK-FST and SK-AST transitions, were characterized by the MOKE-measured m_z–H loops. We also proved that the external field range of the existence of skyrmions could be improved via increasing the diameter of top nanodots d. Moreover, with the help of the FORC technique, we found that the zero-field stability and field range of existence of skyrmions can be improved by choosing the reversal field at the SK region and tailoring d. Finally, according to the asynchronous annihilation of skyrmions, we achieved the zero-field nonvolatile multiple states.

Since its discovery, magnetic skyrmion has been proposed for racetrack memory[16] and logic gate[35] based on the current-driven "continuous" motion along nanowires. Alternatively, the current-driven "local" motion or oscillation of skyrmion in nanodots has also been demonstrated and proposed as microwave nano-oscillators.[47,54,55] Even an electrically configurable pixelated skyrmions on nanoscale magnetic grids has been numerically demonstrated.[81] With the application of electric current, our proposed skyrmions could oscillate in the dots-covered region in the continuous bottom layer and can be used for skyrmion-based microwave nano-oscillators.[47,54,55] In addition, our reported skyrmion states can also be used to produce the zero-field multiple states with memristive behaviors. Hence, both the oscillatory motion and the multistate behavior of our proposed skyrmions could be used for developing future spintronic neuromorphic devices,[82] including nano-oscillator-based magnetic neurons[83,84] and spin-texture-based synapse.[85–87]

IV. METHODS

A. Sample preparation

The used synthetic antiferromagnetic multilayers in this work, Ta(4)/Pt(4)/[Pt(0.6)/Co(0.6)]$_N$/Ru(0.9)/[Co(0.6)/Pt(0.6)]$_4$/Ta(4), were sequentially deposited over oxidized silicon wafers using a DC magnetron sputtering technique. N is 2 or 4 in our work. The numbers in the bracket are the nominal thickness of the corresponding layer. During the deposition, 2.3×10^{-3} Torr Argon gas was filled in the vacuum chamber with a base pressure of 2×10^{-8} Torr. The deposition rates were 0.21, 0.14, and 0.10 Å/s for Co, Pt, and Ru, respectively. The multilayers were then spin-coated with polymethyl methacrylate (PMMA). Electron beam lithography (EBL) was then used to pattern the PMMA layer with circular nanodots. The diameter and spacing of the circular nanodots varied from 100 to 600 nm. Then, Ar^+ ion milling was used to remove the part of the sample above Ru but uncovered by circular PMMA nanodots. Before etching the sputtered SAF multilayers, the etching rates of Ta, Pt, Co, and Ru were separately calibrated and optimized in the AJA ion milling system. During the etching process, the milling process is immediately stopped at a time of t_M when Ru is detected with the help of the element monitor function of the ion milling system. For each t_M, several reference samples were prepared to affirm that the presented samples with the top $[Co/Pt]_4$ layer were fully etched and the bottom $[Pt/Co]_N$ layer was not etched. Finally, we dissolved the remaining PMMA on the sample and obtained patterned nanodots above Ru. The steps above are used to prepare the samples for MOKE measurements. To prepare the samples for Hall resistance measurements, we further etched the Ru layer and the bottom $[Pt/Co]_N$ layer below Ru into a crossbar shape (length 40 μm and width 3 μm) using EBL and Ar^+ ion milling methods. The samples used for MOKE measurements have periodic nanodots, while the samples used for Hall resistance measurements have a single nanodot or nine nanodots as shown in Fig. 1(a).

B. Magneto-optical Kerr effect and Hall resistance measurements

The m_z–H loops and the FORCs were measured by the MagVision Kerr imaging system. Differential imaging technology and piezoelectric actuators were applied to enhance the detected magnetic signal and to eliminate the influence of sample drift, respectively. Refer to https://www.vertisis.com.sg/. The Hall resistance measurements were conducted with an AC/DC source of Keithley 6221 and a nano voltmeter of Keithley 2182A. The current used in all the Hall resistance measurements was a square wave with a peak-to-peak amplitude of 0.2 mA.

Magnetic Force Microscopy: MFM measurements were conducted in a home-built system. This system has a superconducting magnet with a maximum magnetic field of 20 T.[88,89] The piezoresistive cantilever of the system is the commercial PRC400 from Hitachi High-Tech Science Corporation. This cantilever has a 42 kHz resonant frequency. The MFM tip is coated with Cr, Fe, and Au films. The thicknesses of Cr, Fe, and Au coating are 5, 50, and 5 nm, respectively. The coercivity and saturation fields of the MFM tip are $H_c \approx 0.25$ kOe and $H_{sat} \approx 2$ kOe, respectively. The MFM uses a built-in phase-locked loop to adjust the scanning process and process signals. During the MFM measurement, the contact mode was first used to obtain a topographic image. According to the topographic image, the sample surface tilting along the fast and slow scan axes can be compensated. Second, the MFM images were measured in a frequency-modulation mode with a tip height of $\sim$100 nm.

SUPPLEMENTARY MATERIAL

See the supplementary material for additional experimental and simulated results: micromagnetic simulation details; schematics of the samples for MOKE and Hall resistance measurements; definition of the coercive field; strength of antiferromagnetic interlayer exchange coupling; full descending branches of m_z–H loops of nanostructured SAF multilayers; FORC measurement; analysis of the FORC diagram; and asynchronous evolution of skyrmions.

ACKNOWLEDGMENTS

F.M. acknowledges support from the National Natural Science Foundation of China (Grant Nos. 12074189 and 11704191). X.R.W. acknowledges support from Academic Research Fund Tier 2 (Grant Nos. MOE-T2EP50120-0006 and MOE-T2EP50220-0016) and from the Singapore Ministry of Education and Agency for Science, Technology, and Research (A*STAR) under its AME IRG grant (Project No. A20E5c0094). Q.L. and Q.F. acknowledge support from the National Key R&D Program of China (Grant No. 2017YFA0402903), the National Natural Science Foundation of China (Grant Nos. U1932216, 51627901, and 12004386), Hefei Science Center CAS (Grant Nos. 2020HSC-UE014 and 2021HSC-UE010), and the Maintenance and Renovation Project for CAS (Grant No. DSS-WXGZ-2019–0011). W.S.L. acknowledges support from an NRF-CRP Grant (No. CRP9–2011-01), a RIE2020 ASTAR AME IAF-ICP Grant (No. I1801E0030), and an ASTAR AME Programmatic Grant (No. A1687b0033). W.S.L. is a member of the SG-SPIN Consortium.

AUTHOR DECLARATIONS

Conflict of Interest

The authors have no conflicts to disclose.

Author Contributions

M.M. and K.H. contributed equally to this work.

DATA AVAILABILITY

The data that support the findings of this study are available from the corresponding author upon reasonable request.

REFERENCES

[1]T. H. R. Skyrme, Nucl. Phys. **31**, 556 (1962).
[2]A. N. Bogdanov and D. A. Yablonskii, Zh. Eksp. Teor. Fiz. **95**, 178 (1989).
[3]A. N. Bogdanov and A. Hubert, J. Magn. Magn. Mater. **138**, 255 (1994).
[4]U. K. Rößler, A. N. Bogdanov, and C. Pfleiderer, Nature **442**, 797 (2006).
[5]S. Mühlbauer, B. Binz, F. Jonietz, C. Pfleiderer, A. Rosch, A. Neubauer, R. Georgii, and P. Böni, Science **323**, 915 (2009).
[6]I. Dzyaloshinsky, J. Phys. Chem. Solids **4**, 241 (1958).
[7]T. Moriya, Phys. Rev. **120**, 91 (1960).
[8]A. Fert and P. M. Levy, Phys. Rev. Lett. **44**, 1538 (1980).
[9]X. Z. Yu, Y. Onose, N. Kanazawa, J. H. Park, J. H. Han, Y. Matsui, N. Nagaosa, and Y. Tokura, Nature **465**, 901 (2010).
[10]W. Münzer, A. Neubauer, T. Adams, S. Mühlbauer, C. Franz, F. Jonietz, R. Georgii, P. Böni, B. Pedersen, M. Schmidt, A. Rosch, and C. Pfleiderer, Phys. Rev. B **81**, 041203 (2010).
[11]X. Z. Yu, N. Kanazawa, Y. Onose, K. Kimoto, W. Z. Zhang, S. Ishiwata, Y. Matsui, and Y. Tokura, Nat. Mater. **10**, 106 (2011).
[12]N. Romming, C. Hanneken, M. Menzel, J. E. Bickel, B. Wolter, V. Bergmann, A. Kubetzka, and R. Wiesendanger, Science **341**, 636 (2013).
[13]A. O. Leonov, I. E. Dragunov, U. K. Rößler, and A. N. Bogdanov, Phys. Rev. E **90**, 042502 (2014).
[14]M. C. Langner, S. Roy, S. K. Mishra, J. C. T. Lee, X. W. Shi, M. A. Hossain, Y.-D. Chuang, S. Seki, Y. Tokura, S. D. Kevan, and R. W. Schoenlein, Phys. Rev. Lett. **112**, 167202 (2014).
[15]J. Iwasaki, M. Mochizuki, and N. Nagaosa, Nat. Nanotechnol. **8**, 742 (2013).
[16]A. Fert, V. Cros, and J. Sampaio, Nat. Nanotechnol. **8**, 152 (2013).
[17]W. Jiang, P. Upadhyaya, W. Zhang, G. Yu, M. B. Jungfleisch, F. Y. Fradin, J. E. Pearson, Y. Tserkovnyak, K. L. Wang, O. Heinonen, S. G. E. te Velthuis, and A. Hoffmann, Science **349**, 283 (2015).
[18]C. Moreau-Luchaire, C. Moutafis, N. Reyren, J. Sampaio, C. A. F. Vaz, N. Van Horne, K. Bouzehouane, K. Garcia, C. Deranlot, P. Warnicke, P. Wohlhüter, J.-M. George, M. Weigand, J. Raabe, V. Cros, and A. Fert, Nat. Nanotechnol. **11**, 444 (2016).
[19]S. Woo, K. Litzius, B. Krüger, M.-Y. Im, L. Caretta, K. Richter, M. Mann, A. Krone, R. M. Reeve, M. Weigand, P. Agrawal, I. Lemesh, M.-A. Mawass, P. Fischer, M. Kläui, and G. S. D. Beach, Nat. Mater. **15**, 501 (2016).
[20]O. Boulle, J. Vogel, H. Yang, S. Pizzini, D. de Souza Chaves, A. Locatelli, T. Onur Menteş, A. Sala, L. D. Buda-Prejbeanu, O. Klein, M. Belmeguenai, Y. Roussigné, A. Stashkevich, S. M. Chérif, L. Aballe, M. Foerster, M. Chshiev, S. Auffret, I. M. Miron, and G. Gaudin, Nat. Nanotechnol. **11**, 449 (2016).
[21]A. Soumyanarayanan, M. Raju, A. L. Gonzalez Oyarce, A. K. C. Tan, M.-Y. Im, A. P. Petrović, P. Ho, K. H. Khoo, M. Tran, C. K. Gan, F. Ernult, and C. Panagopoulos, Nat. Mater. **16**, 898 (2017).
[22]A. Yagil, A. Almoalem, A. Soumyanarayanan, A. K. C. Tan, M. Raju, C. Panagopoulos, and O. M. Auslaender, Appl. Phys. Lett. **112**, 192403 (2018).
[23]N. Nagaosa and Y. Tokura, Nat. Nanotechnol. **8**, 899 (2013).
[24]J. Barker and O. A. Tretiakov, Phys. Rev. Lett. **116**, 147203 (2016).
[25]A. Fert, N. Reyren, and V. Cros, Nat. Rev. Mater. **2**, 17031 (2017).
[26]K. Everschor-Sitte, J. Masell, R. M. Reeve, and M. Kläui, J. Appl. Phys. **124**, 240901 (2018).
[27]W. Jiang, G. Chen, K. Liu, J. Zang, S. G. te Velthuis, and A. Hoffmann, Phys. Rep. **704**, 1–49 (2017).
[28]X. Zhang, Y. Zhou, K. Mee Song, T.-E. Park, J. Xia, M. Ezawa, X. Liu, W. Zhao, G. Zhao, and S. Woo, J. Phys.: Condens. Matter **32**, 143001 (2020).
[29]C. Back, V. Cros, H. Ebert, K. Everschor-Sitte, A. Fert, M. Garst, T. Ma, S. Mankovsky, T. L. Monchesky, M. Mostovoy, N. Nagaosa, S. S. P. Parkin, C. Pfleiderer, N. Reyren, A. Rosch, Y. Taguchi, Y. Tokura, K. von Bergmann, and J. Zang, J. Phys. D **53**, 363001 (2020).
[30]C. H. Marrows and K. Zeissler, Appl. Phys. Lett. **119**, 250502 (2021).
[31]B. Göbel, I. Mertig, and O. A. Tretiakov, Phys. Rep. **895**, 1–28 (2021).
[32]Z. Chen and F. Ma, J. Appl. Phys. **130**, 090901 (2021).
[33]R. Tomasello, E. Martinez, R. Zivieri, L. Torres, M. Carpentieri, and G. Finocchio, Sci. Rep. **4**, 6784 (2014).
[34]W. Kang, Y. Huang, C. Zheng, W. Lv, N. Lei, Y. Zhang, X. Zhang, Y. Zhou, and W. Zhao, Sci. Rep. **6**, 23164 (2016).
[35]X. Zhang, M. Ezawa, and Y. Zhou, Sci. Rep. **5**, 9400 (2015).
[36]S. Luo, M. Song, X. Li, Y. Zhang, J. Hong, X. Yang, X. Zou, N. Xu, and L. You, Nano Lett. **18**, 1180 (2018).
[37]F. Ma, Y. Zhou, H. B. Braun, and W. S. Lew, Nano Lett. **15**, 4029 (2015).
[38]A. Roldán-Molina, A. S. Nunez, and J. Fernández-Rossier, New J. Phys. **18**, 45015 (2016).
[39]H. Yu, J. Xiao, and H. Schultheiss, Phys. Rep. **905**, 1–59 (2021).
[40]Z.-X. Li, Y. Cao, and P. Yan, Phys. Rep. **915**, 1–64 (2021).
[41]H. Du, R. Che, L. Kong, X. Zhao, C. Jin, C. Wang, J. Yang, W. Ning, R. Li, C. Jin, X. Chen, J. Zang, Y. Zhang, and M. Tian, Nat. Commun. **6**, 8504 (2015).
[42]R. Juge, K. Bairagi, K. G. Rana, J. Vogel, M. Sall, D. Mailly, V. T. Pham, Q. Zhang, N. Sisodia, M. Foerster, L. Aballe, M. Belmeguenai, Y. Roussigné, S. Auffret, L. D. Buda-Prejbeanu, G. Gaudin, D. Ravelosona, and O. Boulle, Nano Lett. **21**, 2989 (2021).
[43]K. Ohara, X. Zhang, Y. Chen, Z. Wei, Y. Ma, J. Xia, Y. Zhou, and X. Liu, Nano Lett. **21**, 4320 (2021).
[44]X. Zhang, M. Ezawa, D. Xiao, G. P. Zhao, Y. Liu, and Y. Zhou, Nanotechnology **26**, 225701 (2015).
[45]X. Zhang, J. Müller, J. Xia, M. Garst, X. Liu, and Y. Zhou, New J. Phys. **19**, 065001 (2017).
[46]Y. Y. Dai, H. Wang, P. Tao, T. Yang, W. J. Ren, and Z. D. Zhang, Phys. Rev. B **88**, 054403 (2013).
[47]L. Shen, J. Xia, G. Zhao, X. Zhang, M. Ezawa, O. A. Tretiakov, X. Liu, and Y. Zhou, Appl. Phys. Lett. **114**, 042402 (2019).
[48]L. Sun, R. X. Cao, B. F. Miao, Z. Feng, B. You, D. Wu, W. Zhang, A. Hu, and H. F. Ding, Phys. Rev. Lett. **110**, 167201 (2013).
[49]J. Li, A. Tan, K. W. Moon, A. Doran, M. A. Marcus, A. T. Young, E. Arenholz, S. Ma, R. F. Yang, C. Hwang, and Z. Q. Qiu, Nat. Commun. **5**, 4704 (2014).
[50]D. A. Gilbert, B. B. Maranville, A. L. Balk, B. J. Kirby, P. Fischer, D. T. Pierce, J. Unguris, J. A. Borchers, and K. Liu, Nat. Commun. **6**, 8462 (2015).
[51]G. Siracusano, R. Tomasello, A. Giordano, V. Puliafito, B. Azzerboni, O. Ozatay, M. Carpentieri, and G. Finocchio, Phys. Rev. Lett. **117**, 087204 (2016).
[52]V. Karakas, A. Gokce, A. T. Habiboglu, S. Arpaci, K. Ozbozduman, I. Cinar, C. Yanik, R. Tomasello, S. Tacchi, G. Siracusano, M. Carpentieri, G. Finocchio, T. Hauet, and O. Ozatay, Sci. Rep. **8**, 7180 (2018).
[53]Y. Li, Q. Feng, S. Li, K. Huang, M. Ma, W. Gan, H. Zhou, X. Jin, X. Renshaw Wang, Y. Lu, W. S. Lew, Q. Lu, and F. Ma, Adv. Funct. Mater. **30**, 1907140 (2020).
[54]S. Zhang, J. Wang, Q. Zheng, Q. Zhu, X. Liu, S. Chen, C. Jin, Q. Liu, C. Jia, and D. Xue, New J. Phys. **17**, 023061 (2015).
[55]F. G. Sanchez, J. Sampaio, N. Reyren, V. Cros, and J.-V. Kim, New J. Phys. **18**, 075011 (2016).
[56]B. F. Miao, L. Sun, Y. W. Wu, X. D. Tao, X. Xiong, Y. Wen, R. X. Cao, P. Wang, D. Wu, Q. F. Zhan, B. You, J. Du, R. W. Li, and H. F. Ding, Phys. Rev. B **90**, 174411 (2014).
[57]H. Z. Wu, B. F. Miao, L. Sun, D. Wu, and H. F. Ding, Phys. Rev. B **95**, 174416 (2017).
[58]R. Streubel, L. Han, M.-Y. Im, F. Kronast, U. K. Rößler, F. Radu, R. Abrudan, G. Lin, O. G. Schmidt, P. Fischer, and D. Makarov, Sci. Rep. **5**, 8787 (2015).
[59]K. Y. Guslienko, IEEE Magn. Lett. **6**, 4000104 (2015).
[60]R. Streubel, P. Fischer, M. Kopte, O. G. Schmidt, and D. Makarov, Appl. Phys. Lett. **107**, 112406 (2015).
[61]N. Del-Valle, S. Agramunt-Puig, A. Sanchez, and C. Navau, Appl. Phys. Lett. **107**, 133103 (2015).
[62]G. Yu, A. Jenkins, X. Ma, S. A. Razavi, C. He, G. Yin, Q. Shao, Q. L. He, H. Wu, W. Li, W. Jiang, X. Han, X. Li, A. C. Bleszynski Jayich, P. K. Amiri, and K. L. Wang, Nano Lett. **18**, 980 (2018).
[63]Y. Guang, Y. Peng, Z. Yan, Y. Liu, J. Zhang, X. Zeng, S. Zhang, S. Zhang, D. M. Burn, N. Jaouen, J. Wei, H. Xu, J. Feng, C. Fang, G. van der Laan, T. Hesjedal, B. Cui, X. Zhang, G. Yu, and X. Han, Adv. Mater. **32**, 2003003 (2020).
[64]Y. Guang, I. Bykova, Y. Liu, G. Yu, E. Goering, M. Weigand, J. Gräfe, S. K. Kim, J. Zhang, H. Zhang, Z. Yan, C. Wan, J. Feng, X. Wang, C. Guo, H. Wei, Y. Peng, Y. Tserkovnyak, X. Han, and G. Schütz, Nat. Commun. **11**, 949 (2020).
[65]X. Zhang, Y. Zhou, and M. Ezawa, Nat. Commun. **7**, 10293 (2016).
[66]X. Zhang, M. Ezawa, and Y. Zhou, Phys. Rev. B **94**, 064406 (2016).
[67]R. Tomasello, V. Puliafito, E. Martinez, A. Manchon, M. Ricci, M. Carpentieri, and G. Finocchio, J. Phys. D **50**, 325302 (2017).

[68]T. Dohi, S. DuttaGupta, S. Fukami, and H. Ohno, Nat. Commun. **10**, 5153 (2019).
[69]W. Legrand, D. Maccariello, F. Ajejas, S. Collin, A. Vecchiola, K. Bouzehouane, N. Reyren, V. Cros, and A. Fert, Nat. Mater. **19**, 34 (2020).
[70]Z. Yu, M. Shen, Z. Zeng, S. Liang, Y. Liu, M. Chen, Z. Zhang, Z. Lu, L. You, X. Yang, Y. Zhang, and R. Xiong, Nanoscale Adv. **2**, 1309 (2020).
[71]O. Hellwig, A. Berger, and E. E. Fullerton, Phys. Rev. Lett. **91**, 197203 (2003).
[72]O. Hellwig, A. Berger, J. B. Kortright, and E. E. Fullerton, J. Magn. Magn. Mater. **319**, 13 (2007).
[73]O. Hellwig, A. Berger, and E. E. Fullerton, Phys. Rev. B **75**, 134416 (2007).
[74]A. Al Subhi and R. Sbiaa, J. Magn. Magn. Mater. **489**, 165460 (2019).
[75]J. E. Davies, O. Hellwig, E. E. Fullerton, G. Denbeaux, J. B. Kortright, and K. Liu, Phys. Rev. B **70**, 224434 (2004).
[76]N. K. Duong, M. Raju, A. P. Petrović, R. Tomasello, G. Finocchio, and C. Panagopoulos, Appl. Phys. Lett. **114**, 072401 (2019).
[77]J. B. Abugri, B. D. Clark, P. B. Visscher, J. Gong, and S. Gupta, J. Appl. Phys. **126**, 013901 (2019).
[78]N. K. Duong, R. Tomasello, M. Raju, A. P. Petrović, S. Chiappini, G. Finocchio, and C. Panagopoulos, APL Mater. **8**, 111112 (2020).
[79]A. K. C. Tan, J. Lourembam, X. Chen, P. Ho, H. K. Tan, and A. Soumyanarayanan, Phys. Rev. Mater. **4**, 114419 (2020).
[80]C. C. I. Ang, W. Gan, G. D. H. Wong, and W. S. Lew, Phys. Rev. B **103**, 144409 (2021).
[81]X. Zhang, J. Xia, K. Shirai, H. Fujiwara, O. A. Tretiakov, M. Ezawa, Y. Zhou, and X. Liu, Commun. Phys. **4**, 255 (2021).
[82]J. Grollier, D. Querlioz, K. Y. Camsari, K. Everschor-Sitte, S. Fukami, and M. D. Stiles, Nat. Electron. **3**, 360 (2020).
[83]A. Sengupta, P. Panda, P. Wijesinghe, Y. Kim, and K. Roy, Sci. Rep. **6**, 30039 (2016).
[84]X. Liang, X. Zhang, J. Xia, M. Ezawa, Y. Zhao, G. Zhao, and Y. Zhou, Appl. Phys. Lett. **116**, 122402 (2020).
[85]S. Lequeux, J. Sampaio, V. Cros, K. Yakushiji, A. Fukushima, R. Matsumoto, H. Kubota, S. Yuasa, and J. Grollier, Sci. Rep. **6**, 31510 (2016).
[86]S. Li, W. Kang, Y. Huang, X. Zhang, Y. Zhou, and W. Zhao, Nanotechnology **28**, 31LT01 (2017).
[87]Y. Huang, W. Kang, X. Zhang, Y. Zhou, and W. Zhao, Nanotechnology **28**, 08LT02 (2017).
[88]H. Zhou, L. Wang, Y. Hou, Z. Huang, Q. Lu, and W. Wu, Nat. Commun. **6**, 8980 (2015).
[89]L. Wang, Q. Feng, Y. Kim, R. Kim, K. H. Lee, S. D. Pollard, Y. J. Shin, H. Zhou, W. Peng, D. Lee, W. Meng, H. Yang, J. H. Han, M. Kim, Q. Lu, and T. W. Noh, Nat. Mater. **17**, 1087 (2018).